

Spectra of Magnoroton and Chiral Graviton Modes of Fractional Chern Insulator

Min Long,¹ Hongyu Lu,¹ Han-Qing Wu,² and Zi Yang Meng^{1,*}

¹*Department of Physics and HK Institute of Quantum Science & Technology,
The University of Hong Kong, Pokfulam Road, Hong Kong*

²*Guangdong Provincial Key Laboratory of Magnetoelectric Physics and Devices,
School of Physics, Sun Yat-sen University, Guangzhou 510275, China*

(Dated: January 9, 2025)

Employing the state-of-the-art time-dependent variational principle algorithm, we compute the spectra of charge neutral excitations in the $\nu = 1/2$ fractional Chern insulator (FCI) on the Haldane honeycomb lattice model with hard-core bosons. The magnoroton visualized from the dynamic density structure factor, acquire a minimum gap at finite momentum that can go soft with increasing interaction and give rise to a charge density wave (CDW) at the same wavevector. The sharper and more concentrated spectral weight of the roton mode is observed when approaching the FCI-CDW transition while the single-particle gap remains intact. We also resolve the graviton mode around Γ point of the Brillouin zone by measuring the dynamic quadrupolar density correlations. Interestingly, we not only reveal the graviton response is chiral for a certain FCI, but also show the different chiralities of the graviton of opposite-sign Hall conductance for the first time. Our results offer the clear spectral observations of magnoroton and chiral graviton in a lattice model of FCI and will have relevance towards the on-going experiments of tunable FCIs in quantum moiré materials.

Introduction.— The fractional quantum Hall effect (FQHE) is one of the most exotic macroscopic quantum phenomena caused by the interplay of electron correlation and topology in modern condensed matter physics [1, 2], where 2D electron gas under strong magnetic field form an incompressible quantum fluid with fractional charge and statistics. The lattice analog of the FQHE is called the fractional Chern insulator (FCI) [3–6], and the zero-magnetic-field FCIs are also known as the fractional quantum anomalous Hall (FQAH) states [4, 7, 8]. The recent breakthroughs in the observations of FQAH states in twisted transition metal dichalcogenide MoTe_2 bilayers [9–12] and in rhombohedral pentalayer graphene/hBN moiré superlattices [13], have attracted broad attentions and the discussions of the properties of these FQAH states and their transitions to charge density wave (CDW) state, metallic state and various anomalous Hall crystal states are actively undertaking [14–19].

FCIs have been studied in many aspects in connection with FQHE, including the similarity and difference between topological flat bands and Landau levels [20–23], the correspondence between their wave functions [24] and the ground state entanglement and generalized Pauli principle [6]. As for the collective excitations, the charge-neutral excitations are known to play a dominant role in controlling the properties of the FQHE/FCI systems. For example, the softening of magnoroton (minimum) is an intrinsic mechanism to trigger phase transitions from FQHE/FCI to CDW [4, 25–34]. The magnoroton in the long-wavelength limit is known as the chiral graviton [35], reflecting the oscillation of the geometrical properties, which carries the spin angular momentum 2 [36–41]. This geometrical (apart from the topological) description of the FQHE was proposed by Haldane [42] and the experimental observation of chiral gravitons of FQH states was recently reported [43]. Similar as the roton minimum, the graviton mode could also approach the ground-state energy which leads to the FQH nematic state with anisotropic transport [44–

47] and describe quench dynamics [48, 49].

In the past, the dynamic (spectral) properties of FCI are mainly studied in projected topological flat band, mimic the investigations of the charge neutral excitations with Landau level projection in FQHE [33–35, 37, 39, 41, 45, 51–53]. While the universal properties could be undoubtedly studied in this way, the dynamics are model dependent and largely affected by band mixing, which could destroy FCI by quantum fluctuation and might be responsible for the sharp difference of the particle-hole fillings of the same Chern band in experiments [13, 54, 55]. Moreover, previous studies of the dynamic properties of FCI focused on the charge excitations [56], which is typically of a higher energy scale compared with neutral excitations. Although the single mode approximation (SMA) was done for FCI (projecting to one Chern band and no spectrum weight) [52], the low-lying dispersions with the identification of roton minimum were not clear without mapping the quantum numbers of momenta between discrete lattices and continuum models, which was model-dependent, and the importance of the spectrum weight has not been revealed. While the energy scale of different excitations in FCI has been discussed through thermodynamic calculation [25, 26], a comprehensive study of the dynamic properties of FCI is still lacking. However, it is well understood that such direct and spectroscopic evidence for the presence of magnorotons and chiral gravitons, will be of great importance to guide future experiments and provide unbiased verifications for the developments of unifying theories for FQHE and FCI systems.

In this letter, we fill in such a knowledge gap by studying the spectral properties of FCI realised by hard-core bosons on Haldane honeycomb lattice model at half filling of the flat band [4, 5]. And the FCI therein can transit to two CDW phases as a function of the repulsive density-density interaction [29]. We employ the state-of-the-art time-dependent variational principle (TDVP) [57, 58] within large-scale density ma-

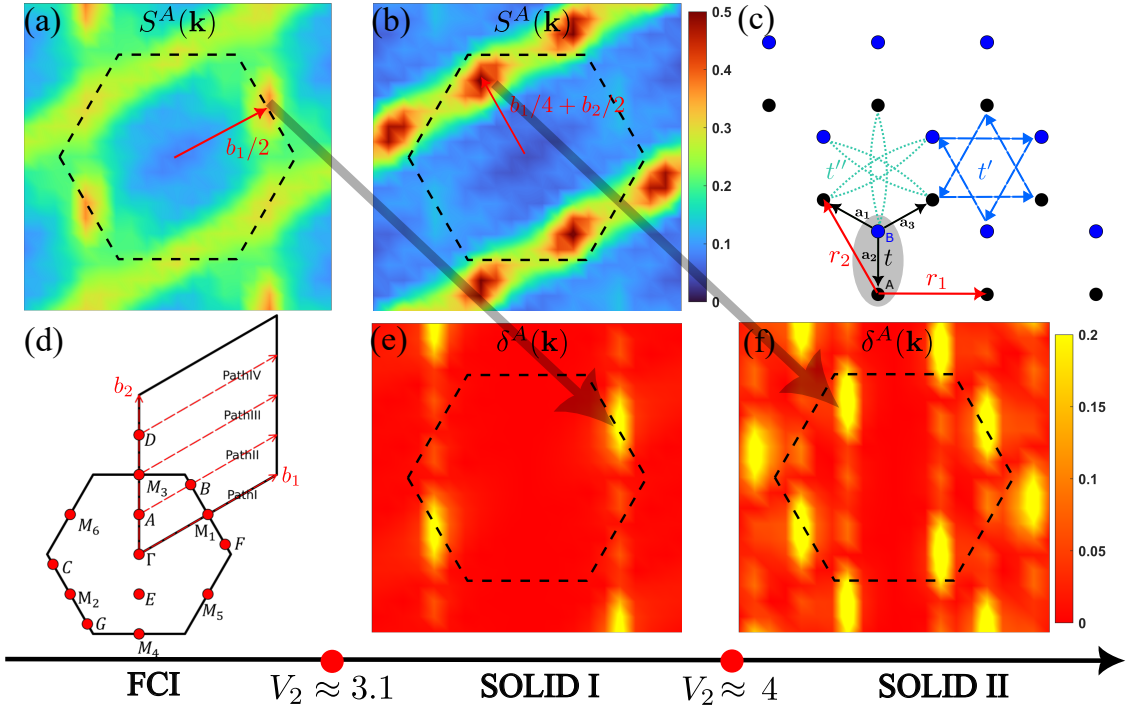


Figure 1. **Static density structure factor $S^A(\mathbf{k})$ and charge order parameter $\delta^A(\mathbf{k})$.** Along the parameter path we choose, the system undergoes a sequence of FCI-Solid I-Solid II phase transitions. (a), (b) are the $S^A(\mathbf{k})$ of FCI phase ($V_1 = 4, V_2 = 2.5$) and Solid I phase ($V_1 = 4, V_2 = 3.2$). (c), (d) are the real and reciprocal spaces of the honeycomb lattice FCI model in Eq. (1). In (c), $\mathbf{r}_1 = (\sqrt{3}, 0)$, $\mathbf{r}_2 = (-\sqrt{3}/2, 3/2)$ are the primitive lattice vectors. The NN, NNN, and NNNN hoppings are depicted with black, blue and green colours, respectively. In (d), the solid hexagon is the first Brillouin zone (BZ) of the model, with high symmetry points labelled. The four paths that are discrete in \mathbf{b}_2 direction with step $\mathbf{b}_2/4$ are where we compute the spectra under the cylinder geometry in DMRG calculation. (e), (f) are the $\delta^A(\mathbf{k})$ of Solid I phase ($V_1 = 4, V_2 = 3.2$) and Solid II phase ($V_1 = 4, V_2 = 4.6$). The roton mode locates at $\mathbf{b}_1/2$ in (a) condensates and leads to charge order in (e), while similar $\mathbf{b}_1/4 + \mathbf{b}_2/2$ roton in (b) condensates and give rise to the charge order in (f). The data that determine of the transition points are given in Supplemental Material (SM) [50].

trix renormalization group (DMRG) simulation [59] to reveal the spectroscopic signatures for the FCI state and its transition to CDW orders. We find that (1) the charge neutral magnetoroton can be visualized from the dynamic density structure factor. The roton mode could go soft and finally leads to the CDW order of the same momentum as the roton minimum, whereas the single-particle gap remains large and intact throughout; (2) The spectral weight of roton become sharper and highly concentrated around its minimum when approaching the phase boundary, manifesting the roton condensation character of the FCI-CDW transition; (3) Inside the FCI, a strong gapped chiral graviton mode – probed by quadrupolar density correlation function – with angular momentum-2 is clearly present and its chirality can be tuned by flipping the Chern number ± 1 of the flat band. Our results shows, in an unbiased manner, the robustness and tunability of the charge neutral excitations in the FCI states and provide guidance towards their spectroscopic detection in quantum moiré materials.

Model and Method.— We consider the bosonic topological

flat band Hamiltonian on honeycomb lattice [4, 5, 29]:

$$\begin{aligned}
 H = & -t \sum_{\langle i,j \rangle} \left(b_i^\dagger b_j e^{i\phi_{ij}} + \text{H.c.} \right) - t' \sum_{\langle\langle i,j \rangle\rangle} \left(b_i^\dagger b_j + \text{H.c.} \right) \\
 & - t'' \sum_{\langle\langle\langle i,j \rangle\rangle\rangle} \left(b_i^\dagger b_j + \text{H.c.} \right) + V_1 \sum_{\langle i,j \rangle} n_i n_j + V_2 \sum_{\langle\langle i,j \rangle\rangle} n_i n_j,
 \end{aligned} \tag{1}$$

where b_i^\dagger creates a hard core boson at site i , $\langle \dots \rangle$, $\langle\langle \dots \rangle\rangle$, and $\langle\langle\langle \dots \rangle\rangle\rangle$ denote the nearest neighbour (NN), next nearest neighbour (NNN) and next next nearest neighbour (NNNN) sites, respectively, as shown in Fig. 1 (c).

To obtain the flat band with Chern number $C = 1$, we set $t = 1$ (energy unit throughout the paper), $t' = 0.6$, $\phi = \pm 0.4\pi$ and $t'' = -0.58$, following the literature [4, 5, 29]. $V_1(V_2)$ refers to the amplitude of NN (NNN) repulsive interactions. We note that even without the neighboring interaction terms in Eq. (1), the model still hosts a $1/2$ bosonic FCI when the flat band is half filled, which is attributed to the hard-core condition as an infinite on-site repulsion V_0 .

In our simulation, we consider a finite cylinder with $N_1 \times N_2 = 4 \times 16$ unit cells. The total number of sites is $N = 2N_1N_2$ corresponding bosons particle number of $1/2$ fills the flat band is $N_b = N_1N_2/2 = 32$. The details of the cylinder

geometry and simulations is described in SM [50].

Before discussing the spectra, we begin with the ground state phase diagram as shown in Fig. 1. The system goes through a FCI-Solid I-Solid II phase transition triggered by the condensation of two successive rotors (with momenta $\mathbf{b}_1/2$ and $\mathbf{b}_1/4 + \mathbf{b}_2/2$ respectively) as we increase V_2 along the path $V_1 = 4$. Such successive phase transition can be interpreted as a vestigial transition [60–65] with the translational symmetry of the lattice broken in a two-step manner [29]. Here, static density structure factor $S^A(\mathbf{k}) = \frac{1}{N_A} \sum_{ij} e^{-i\mathbf{k}\cdot(\mathbf{x}_i - \mathbf{x}_j)} \langle n_{i,A} n_{j,A} \rangle$ and charge order parameter $\delta^A(\mathbf{k}) = \frac{1}{\sqrt{N_A}} \sum_i e^{-i\mathbf{k}\cdot\mathbf{x}_i} \langle n_{i,A} \rangle$ are measured to diagnose the phases, where A denotes the sub-lattice, N_A denotes its site number, i, j run over all unit cells. Since the results are the same for both sublattices, we mainly present the results on A sublattice. The bright point at $\frac{\mathbf{b}_1}{2}$ in Fig. 1 (a) denotes the location of the lowest roton minimal of FCI [25, 26, 29], the fact that the rotational symmetry is not recovered in the $S^A(\mathbf{k})$ is a consequence of the cylindrical geometry of the DMRG simulation. In this system there is a second roton in the FCI phase, and it is located at the $\mathbf{b}_1/4 + \mathbf{b}_2/2$ (it can be clearly visualised in the spectra in Fig. 2 (b)), and once the lowest roton condenses and the system enters the Solid I phase, the measurement of $S^A(\mathbf{k})$ in Fig. 1 (b) shows that the brightest density correlation is at this wave vector ($V_1 = 4, V_2 = 3.2$). The charge order of Solid I, however, can be seen from its order parameter $\delta^A(\mathbf{k})$ in Fig. 1 (e) ($V_1 = 4, V_2 = 3.2$). And the grey arrow connecting the momentum $\mathbf{b}_1/2$ from Fig. 1 (a) to Fig. 1 (e), symbolises the condensation of the roton and formation of the charge order. The process also happened in transition from Solid I to Solid II, symbolised by the grey arrow connecting the momentum $\mathbf{b}_1/4 + \mathbf{b}_2/2$ of the second roton in Fig. 1 (b) to the charge order in Fig. 1 (f) ($V_1 = 4, V_2 = 4.6$). **Magnetorotons.**—With the ground state phase diagram at hand, we now investigate the spectra of magnetoroton in our system. The dynamic density structure factor is defined as:

$$S^A(\mathbf{k}, \omega) = \frac{1}{\sqrt{N_t N_A}} \sum_{jl} e^{i(\omega + i\eta)t_l} e^{-i\mathbf{k}\cdot(\mathbf{x}_j - \mathbf{x}_0)} (\langle n_{j,A}(t_l) n_{0,A} \rangle - \langle n_{j,A} \rangle \langle n_{0,A} \rangle) \quad (2)$$

where $n_{j,A}(t_l) = e^{iHl\Delta t} n_{j,A} e^{-iHl\Delta t}$ as l runs from 0 to N_t and $\eta = 0.05$. We time evolve $n_{0,A}|\psi_0\rangle$ with $|\psi_0\rangle$ the ground state wave function and $n_{0,A}$ defined in the bulk of the cylinder [50]. The correlation function $\langle \hat{n}_{j,A}(t) \hat{n}_{0,A} \rangle$ is measured at every time slice as we progressively evolve $n_{0,A}|\psi_0\rangle$ with operator e^{-iHt} in TDVP. For $N_t, n_{0,A}$ and the details of spectrum calculation, see SM [50]. We also measure the single-particle Green's functions $\langle b_{j,A}(t_l) b_{0,A}^\dagger \rangle$ and $\langle b_{j,A}^\dagger(t_l) b_{0,A} \rangle$ respectively and label the corresponding spectra with $G_e^A(\mathbf{k}, \omega)$ (electron) and $G_h^A(\mathbf{k}, \omega)$ (hole). We sum $G_e^A(\mathbf{k}, \omega)$ and $G_h^A(-\mathbf{k}, -\omega)$ to obtain single-particle spectrum $G^A(\mathbf{k}, \omega)$, where we use the particle-hole conjugation relation to reverse the sign of momentum and energy for holes. Again b^\dagger and b locate at the bulk of the cylinder.

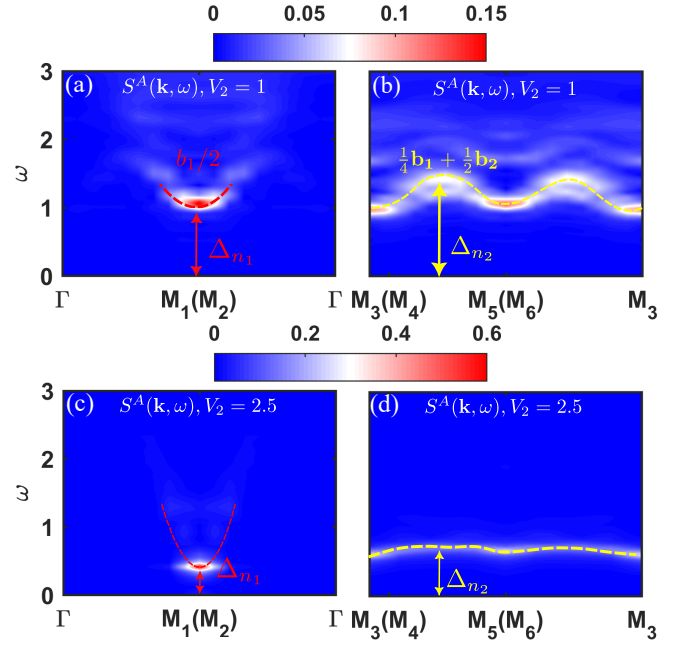


Figure 2. **Magnetoroton spectrum inside FCI phase.** (a), (b) are $S^A(\mathbf{k}, \omega)$ deep inside FCI with $V_1 = 4, V_2 = 1$ along Path I and Path III in Fig. 1 (d). Two charge neutral rotors relevant with the CDW phases are marked with Δ_{n_1} and Δ_{n_2} with their gaps denoted by the red and yellow arrows, respectively. The dashed lines trace the dispersion relation of roton. (c) and (d) are the roton spectra near the FCI-Solid I phase boundary with $V_1 = 4, V_2 = 2.5$. The Δ_{n_1} is about to close with very sharp spectral weight and give rise to the Solid I phase with the charge order at same momentum. The Δ_{n_2} will persist into the Solid I phase and condense at the Solid I - Solid II transition (discussed in Fig. 1 (b) and (f)).

The local density of state can then be obtained as $\rho(\omega) = \frac{1}{N_k} \sum_{\mathbf{k}} G^A(\mathbf{k}, \omega)$.

Fig. 2 shows the $S^A(\mathbf{k}, \omega)$ along the path I and III in the BZ in Fig. 1 (d). Panels (a) and (b) of Fig. 2 are deep inside the FCI phase, and one clearly sees the lowest roton minimal at M_1 with the roton gap $\Delta_{n_1} \sim 1$, which is much smaller than the single-particle gap computed at the same parameter which is $\Delta_c \sim 2$ with sharper spectrum weight, as shown in Fig. 3 (a). This observation further reinforces the understanding that in the FCI phase, the lowest excitations are the charge neutral roton instead of the single-particle ones [25]. Panel (b) exhibits the similar lowest rotors at M_3 and M_5 , but more interestingly, there is another higher energy roton manifesting at momentum $\mathbf{b}_1/4 + \mathbf{b}_2/2$, this is the second roton that will trigger the vestigial transition from Solid I to Solid II, once the lowest roton Δ_{n_1} condense to give rise to the Solid I. In Fig. 2 (c) and (d), the parameter ($V_1 = 4, V_2 = 2.5$) is closer to the FCI-Solid I transition, and one sees that the roton gap Δ_{n_1} becomes smaller, signifying the approaching transition.

We note that as the roton is about to condense, its spectral weight become much sharper and concentrated close to its minimum compared with that deep inside the FCI state, we expect such clear dynamic response of the magnetoroton

of FCI close to its transition to CDW phase, can be seen in the future scanning tunneling spectroscopy (STS) or nano-ARPES experiments. Moreover, our previous thermodynamic calculation showed that, in the correlated flat band systems, close to the energy scale of the neutral gap, the compressibility of the system is greatly enhanced [25, 27, 29, 66, 67], here one sees similar proliferation of the roton excitation happen at the FCI-CDW transition and expects there will be strong signal in the compressibility which can be probed from the quantum capacitance experiment.

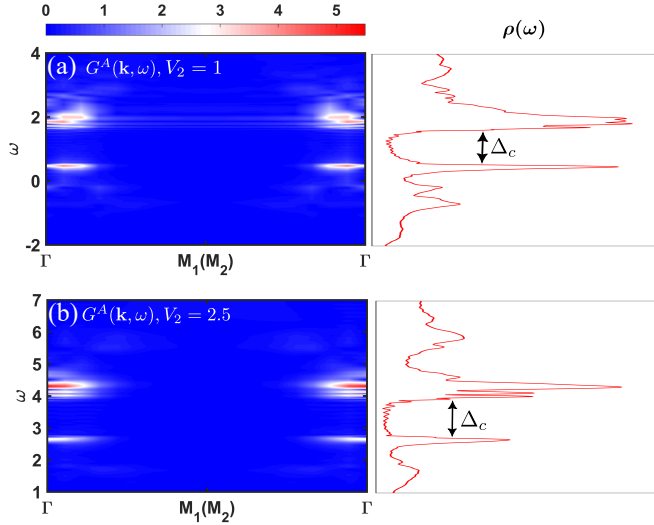


Figure 3. **Single-particle spectrum inside the FCI phase.** (a), (b) are the $G^A(\mathbf{k}, \omega)$ and $\rho(\omega)$ inside the FCI phase (with the same parameter as Fig. 2 (a) and (b) and close to the FCI-Solid I transition (with the same parameter as Fig. 2 (c) and (d)), respectively. In both cases, the single-particle gap $\Delta_c \approx 2$ are much larger than the roton gaps Δ_{n_1} and Δ_{n_2} . The path (Path I) we have chosen to display the single-particle spectrum features a minimal charge gap and encompasses major of the total spectral weight.

We also monitor the evolution of the single-particle spectra along the same parameter path, and the results are shown in Fig. 3. We plot $G^A(\mathbf{k}, \omega)$ and $\rho(\omega)$ in Fig. 3 (a) with $V_2 = 1$ (well inside the FCI phase) and Fig. 3 (b) with $V_2 = 2.5$ (close to the FCI-Solid I transition). It is clear that at both parameters, the single-particle gaps are well developed and much larger than the roton gaps at the same parameter. Such results suggest that, the transition out of a FCI can be purely driven by the charge-neutral roton modes, without the closing of the single-particle gap [26–29].

As shown in Fig. 2 (a) and (c), the chiral graviton mode (CGM) is invisible in $S^A(\mathbf{k}, \omega)$, to investigate CGM in our FCI system, we proceed to compute the dynamic quadrupolar correlation function, as we now turn to.

Chiral Gravitons.— The operators for measuring CGM in lattice are given by the representation of d -wave operators with angular momentum-2 along the NN bonds, $d_{x^2-y^2} = \sum_i n_{r_i} n_{r_i+a_1} - \frac{1}{2} n_{r_i} n_{r_i+a_2} - \frac{1}{2} n_{r_i} n_{r_i+a_3}$ and $d_{xy} = \sum_i \frac{\sqrt{3}}{2} (n_{r_i} n_{r_i+a_2} - n_i n_{r_i+a_3})$, where the form factor de-

pends on the unit vector $\mathbf{a}_{i=1,2,3}$ as depicted in Fig. 1 (c). The chiral density operator $O^\pm = d_{x^2-y^2} \pm i d_{xy}$ is constructed from the d -wave operators that is angular momentum $S = 2$ or $S = -2$ under chiral transformation [40, 41]. We therefore define the dynamic quadrupolar density correlation function as

$$g^\pm(\mathbf{k}, \omega) = \frac{1}{\sqrt{N_t N_A}} \sum_{jl} e^{i\omega t_l} e^{-i\mathbf{k} \cdot (\mathbf{x}_j - \mathbf{x}_0)} \langle (O_{j,A}^\pm(t_l))^\dagger O_{0,A}^\pm \rangle - \langle (O_{j,A}^\pm)^\dagger \rangle \langle O_{0,A}^\pm \rangle \quad (3)$$

with $(O^\pm)^\dagger = O^\mp$.

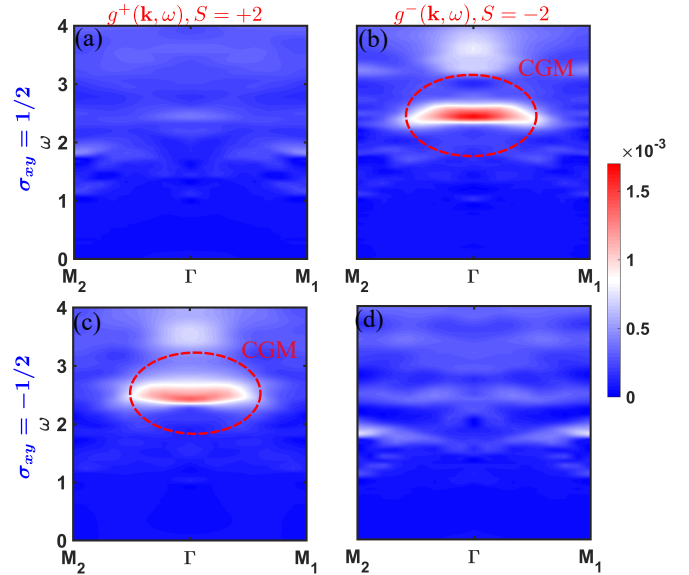


Figure 4. **Chiral graviton mode (CGM) inside FCI phase ($V_1 = 4, V_2 = 1$) and its tunability.** (a) and (b) are the dynamic quadrupolar density correlations g^+ ($S = 2$) and g^- ($S = -2$), respectively. The chiral $S = -2$ graviton extends around Γ point (denoted by the red dashed ellipse). In (c) and (d), we revert the magnetic flux ϕ such that the Chern number for lower band is $C = -1$ and calculate g^+ and g^- as in (a) and (b). The chirality of the graviton mode is clearly reversed.

Fig. 4 (a) and (b) are the $g^+(\mathbf{k}, \omega)$ and $g^-(\mathbf{k}, \omega)$ at $V_1 = 0, V_2 = 0$ inside the FCI phase. One sees a strong charge neutral response close to the momentum Γ at ($S = -2$) sector. This is also the momenta where the CGM was proposed in the FQHE literature [35, 68] and experiment [43]. One more interesting analysis we did here is to switch the Chern number and chirality of the flat band in our model, this is similar with the observation of the CGM in the FQHE experiment that hole doping FQHE state ($\nu = 2/3$) have opposite chirality compared with it's electron ($\nu = 1/3$) counterpart. As shown in Fig. 4 (c) and (d), once we revert the flux directions in the in the t' -term in Eq. (1), at the same interaction strength of FCI phase, the graviton appears near the Γ point in $g^+(\mathbf{k}, \omega)$. The CGM at finite momentum could lead to spatial modulation of internal quantum metric and more easily captured by experiment. We think such tunability of the chirality of the

graviton in the FCI system could be potentially observed in the circularly polarized resonant inelastic light scattering experiment [43, 69].

Discussion.— In this work, we observe the clear spectral properties of the magnetoroton and chiral graviton, as the collective charge neutral excitations in FCI system. We discover that the roton minimum can go soft and give rise to a CDW phase (with the corresponding wavevector), while during the process, the spectral weight of the roton excitation become sharper and more concentrated but the single-particle gap remains large. The enhanced spectral signature and the potentially associated enhanced charge compressibility, are expected to be measured in STS and quantum capacitance experiments. Moreover, we not only show the graviton mode is chiral for a given FCI, but also directly visualize the different chiralities of the CGM of FCIs by tuning the sign of Hall conductance and such novel phenomena can potentially be seen via the resonant inelastic light scattering, as has recently been seen in FQHE experiment [43].

Acknowledgments— We thank Yang Liu, Yuzhu Wang, Bin-Bin Chen, Bo Yang, Wei Zhu, Wang Yao and Di Xiao for helpful discussions. ML, HYL and ZYM acknowledge the support from the Research Grants Council (RGC) of Hong Kong (Project Nos. AoE/P-701/20, 17309822, HKU C7037-22GF, 17302223, 17301924), the ANR/RGC Joint Research Scheme sponsored by RGC of Hong Kong and French National Research Agency (Project No. A_HKU703/22) and the HKU Seed Funding for Strategic Interdisciplinary Research “Many-body paradigm in quantum moiré material research”. We thank HPC2021 system under the Information Technology Services and the Blackbody HPC system at the Department of Physics, University of Hong Kong, as well as the Beijing PARATERA Tech CO.,Ltd. (URL: <https://cloud.paratera.com>) for providing HPC resources that have contributed to the research results reported within this paper. H.Q. Wu acknowledge the support from the National Natural Science Foundation of China (Grant No. 12474248), Guangdong Basic and Applied Basic Research Foundation (Grant No. 2023B1515120013).

Note Added— Upon the completion of our work, we became aware of Ref. [70] which described the neutral excitations of FCI in the continuum model by exact diagonalizations and SMA.

* zymeng@hku.hk

- [1] R. B. Laughlin, *Physical Review Letters* **50**, 1395–1398 (1983).
- [2] D. C. Tsui, H. L. Stormer, and A. C. Gossard, *Physical Review Letters* **48**, 1559–1562 (1982).
- [3] S. A. Parameswaran, R. Roy, and S. L. Sondhi, *Comptes Rendus. Physique* **14**, 816–839 (2013).
- [4] D. Sheng, Z.-C. Gu, K. Sun, and L. Sheng, *Nature Communications* **2**, 10.1038/ncomms1380 (2011).
- [5] Y.-F. Wang, Z.-C. Gu, C.-D. Gong, and D. N. Sheng, *Phys. Rev. Lett.* **107**, 146803 (2011).
- [6] N. Regnault and B. A. Bernevig, *Phys. Rev. X* **1**, 021014 (2011).
- [7] T. Neupert, L. Santos, C. Chamon, and C. Mudry, *Phys. Rev. Lett.* **106**, 236804 (2011).
- [8] E. Tang, J.-W. Mei, and X.-G. Wen, *Phys. Rev. Lett.* **106**, 236802 (2011).
- [9] J. Cai, E. Anderson, C. Wang, X. Zhang, X. Liu, W. Holtzmann, Y. Zhang, F. Fan, T. Taniguchi, K. Watanabe, Y. Ran, T. Cao, L. Fu, D. Xiao, W. Yao, and X. Xu, *Nature* **622**, 63–68 (2023).
- [10] Y. Zeng, Z. Xia, K. Kang, J. Zhu, P. Knüppel, C. Vaswani, K. Watanabe, T. Taniguchi, K. F. Mak, and J. Shan, *Nature* **622**, 69 (2023).
- [11] F. Xu, Z. Sun, T. Jia, C. Liu, C. Xu, C. Li, Y. Gu, K. Watanabe, T. Taniguchi, B. Tong, J. Jia, Z. Shi, S. Jiang, Y. Zhang, X. Liu, and T. Li, *Phys. Rev. X* **13**, 031037 (2023).
- [12] H. Park, J. Cai, E. Anderson, Y. Zhang, J. Zhu, X. Liu, C. Wang, W. Holtzmann, C. Hu, Z. Liu, T. Taniguchi, K. Watanabe, J.-H. Chu, T. Cao, L. Fu, W. Yao, C.-Z. Chang, D. Cobden, D. Xiao, and X. Xu, *Nature* **622**, 74 (2023).
- [13] Z. Lu, T. Han, Y. Yao, A. P. Reddy, J. Yang, J. Seo, K. Watanabe, T. Taniguchi, L. Fu, and L. Ju, *Nature* **626**, 759 (2024).
- [14] J. Dong, T. Wang, T. Wang, T. Soejima, M. P. Zaletel, A. Vishwanath, and D. E. Parker, *Phys. Rev. Lett.* **133**, 206503 (2024).
- [15] T. Soejima, J. Dong, T. Wang, T. Wang, M. P. Zaletel, A. Vishwanath, and D. E. Parker, *Phys. Rev. B* **110**, 205124 (2024).
- [16] Z. Dong, A. S. Patri, and T. Senthil, *Phys. Rev. Lett.* **133**, 206502 (2024).
- [17] D. N. Sheng, A. P. Reddy, A. Abouelkomsan, E. J. Bergholtz, and L. Fu, *Phys. Rev. Lett.* **133**, 066601 (2024).
- [18] Z. Lu, T. Han, Y. Yao, J. Yang, J. Seo, L. Shi, S. Ye, K. Watanabe, T. Taniguchi, and L. Ju, *arXiv e-prints*, [arXiv:2408.10203](https://arxiv.org/abs/2408.10203) (2024), [arXiv:2408.10203 \[cond-mat.mes-hall\]](https://arxiv.org/abs/2408.10203).
- [19] X.-Y. Song, Y.-H. Zhang, and T. Senthil, *Phys. Rev. B* **109**, 085143 (2024).
- [20] G. Murthy and R. Shankar, *Phys. Rev. B* **86**, 195146 (2012).
- [21] J. Wang, J. Cano, A. J. Millis, Z. Liu, and B. Yang, *Phys. Rev. Lett.* **127**, 246403 (2021).
- [22] R. Roy, *Phys. Rev. B* **90**, 165139 (2014).
- [23] S. A. Parameswaran, R. Roy, and S. L. Sondhi, *Phys. Rev. B* **85**, 241308 (2012).
- [24] X.-L. Qi, *Phys. Rev. Lett.* **107**, 126803 (2011).
- [25] H. Lu, B.-B. Chen, H.-Q. Wu, K. Sun, and Z. Y. Meng, *Phys. Rev. Lett.* **132**, 236502 (2024).
- [26] H. Lu, H.-Q. Wu, B.-B. Chen, K. Sun, and Z. Y. Meng, *arXiv e-prints*, [arXiv:2403.03258](https://arxiv.org/abs/2403.03258) (2024), [arXiv:2403.03258 \[cond-mat.str-el\]](https://arxiv.org/abs/2403.03258).
- [27] H. Lu, H.-Q. Wu, B.-B. Chen, and Z. Y. Meng, *arXiv e-prints*, [arXiv:2404.06745](https://arxiv.org/abs/2404.06745) (2024), [arXiv:2404.06745 \[cond-mat.str-el\]](https://arxiv.org/abs/2404.06745).
- [28] H. Lu, H.-Q. Wu, B.-B. Chen, K. Sun, and Z. Y. Meng, *Reports on Progress in Physics* **87**, 108003 (2024).
- [29] H. Lu, H.-Q. Wu, B.-B. Chen, and Z. Y. Meng, *arXiv e-prints*, [arXiv:2408.07111](https://arxiv.org/abs/2408.07111) (2024), [arXiv:2408.07111 \[cond-mat.mes-hall\]](https://arxiv.org/abs/2408.07111).
- [30] W.-W. Luo, A.-L. He, Y. Zhou, Y.-F. Wang, and C.-D. Gong, *Phys. Rev. B* **102**, 155120 (2020).
- [31] H. Wang, R. Narayanan, X. Wan, and F. Zhang, *Phys. Rev. B* **86**, 035122 (2012).
- [32] Y.-F. Wang, H. Yao, Z.-C. Gu, C.-D. Gong, and D. N. Sheng, *Physical Review Letters* **108**, 10.1103/physrevlett.108.126805 (2012).
- [33] S. M. Girvin, A. H. MacDonald, and P. M. Platzman, *Physical Review Letters* **54**, 581–583 (1985).
- [34] P. Kumar and R. N. Bhatt, *Phys. Rev. B* **106**, 115101 (2022).
- [35] B. Yang, Z.-X. Hu, Z. Papić, and F. D. M. Haldane, *Phys. Rev.*

- Lett. **108**, 256807 (2012).
- [36] R.-Z. Qiu, F. D. M. Haldane, X. Wan, K. Yang, and S. Yi, *Phys. Rev. B* **85**, 115308 (2012).
- [37] S.-F. Liou, F. D. M. Haldane, K. Yang, and E. H. Rezayi, *Phys. Rev. Lett.* **123**, 146801 (2019).
- [38] S. Johri, Z. Papić, P. Schmitteckert, R. N. Bhatt, and F. D. M. Haldane, *New Journal of Physics* **18**, 025011 (2016).
- [39] F. D. M. Haldane, E. H. Rezayi, and K. Yang, *Phys. Rev. B* **104**, L121106 (2021).
- [40] S.-F. Liou, F. D. M. Haldane, K. Yang, and E. H. Rezayi, *Phys. Rev. Lett.* **123**, 146801 (2019).
- [41] Y. Wang and B. Yang, *Phys. Rev. B* **105**, 035144 (2022).
- [42] F. D. M. Haldane, *Phys. Rev. Lett.* **107**, 116801 (2011).
- [43] J. Liang, Z. Liu, Z. Yang, Y. Huang, U. Wurstbauer, C. R. Dean, K. W. West, L. N. Pfeiffer, L. Du, and A. Pinczuk, *Nature* **628**, 78–83 (2024).
- [44] J. Xia, J. P. Eisenstein, L. N. Pfeiffer, and K. W. West, *Nature Physics* **7**, 845–848 (2011).
- [45] B. Yang, *Phys. Rev. Res.* **2**, 033362 (2020).
- [46] S. Pu, A. C. Balram, J. Taylor, E. Fradkin, and Z. Papić, *Phys. Rev. Lett.* **132**, 236503 (2024).
- [47] N. Regnault, J. Maciejko, S. A. Kivelson, and S. L. Sondhi, *Phys. Rev. B* **96**, 035150 (2017).
- [48] Z. Liu, A. Gromov, and Z. Papić, *Phys. Rev. B* **98**, 155140 (2018).
- [49] A. C. Balram, Z. Liu, A. Gromov, and Z. Papić, *Phys. Rev. X* **12**, 021008 (2022).
- [50] Sm, in this supplemental material, we provide the details of DMRG and TDVP implementations, more data about the ground state phase diagram of our FCI model, focusing on the FCI-Solid I and Solid I-Solid II transitions, and the spectra of the charge neutral modes, single-particle mode along different paths other than those shown in the main text and benchmark with exact diagonalization.
- [51] F. D. M. Haldane and E. H. Rezayi, *Physical Review Letters* **54**, 237–240 (1985).
- [52] C. Repellin, T. Neupert, Z. Papić, and N. Regnault, *Phys. Rev. B* **90**, 045114 (2014).
- [53] Y. Liu, T. Zhao, and T. Xiang, *Phys. Rev. B* **110**, 195137 (2024).
- [54] J. Yu, J. Herzog-Arbeitman, Y. H. Kwan, N. Regnault, and B. A. Bernevig, *arXiv e-prints*, arXiv:2407.13770 (2024), arXiv:2407.13770 [cond-mat.str-el].
- [55] A. Abouelkomsan, A. P. Reddy, L. Fu, and E. J. Bergholtz, *Phys. Rev. B* **109**, L121107 (2024).
- [56] X.-Y. Dong, A. G. Grushin, J. Motruk, and F. Pollmann, *Phys. Rev. Lett.* **121**, 086401 (2018).
- [57] J. Haegeman, J. I. Cirac, T. J. Osborne, I. Pižorn, H. Verschelde, and F. Verstraete, *Phys. Rev. Lett.* **107**, 070601 (2011).
- [58] J. Haegeman, C. Lubich, I. Oseledets, B. Vandereycken, and F. Verstraete, *Phys. Rev. B* **94**, 165116 (2016).
- [59] S. R. White, *Phys. Rev. Lett.* **69**, 2863 (1992).
- [60] L. Nie, A. V. Maharaj, E. Fradkin, and S. A. Kivelson, *Phys. Rev. B* **96**, 085142 (2017).
- [61] R. M. Fernandes, P. P. Orth, and J. Schmalian, *Annual Review of Condensed Matter Physics* **10**, 133 (2019).
- [62] Y.-C. Wang, Z. Yan, C. Wang, Y. Qi, and Z. Y. Meng, *Phys. Rev. B* **103**, 014408 (2021).
- [63] Z. Sun, G. Ye, M. Huang, C. Zhou, N. Huang, Q. Li, Z. Ye, C. Nnokwe, H. Deng, D. Mandrus, Z. Y. Meng, K. Sun, C. Du, R. He, and L. Zhao, *Nature Physics* **20**, 1764 (2024).
- [64] B. V. Svistunov, E. S. Babaev, and N. V. Prokof'ev, *Superfluid states of matter* (Crc Press, 2015).
- [65] V. Grinenko, D. Weston, F. Caglieris, C. Wuttke, C. Hess, T. Gottschall, I. Maccari, D. Gorbunov, S. Zherlitsyn, J. Wosnitzer, et al., *Nature Physics* **17**, 1254 (2021).
- [66] G. Pan, X. Zhang, H. Lu, H. Li, B.-B. Chen, K. Sun, and Z. Y. Meng, *Phys. Rev. Lett.* **130**, 016401 (2023).
- [67] X. Lin, B.-B. Chen, W. Li, Z. Y. Meng, and T. Shi, *Phys. Rev. Lett.* **128**, 157201 (2022).
- [68] S. Golkar, D. X. Nguyen, and D. T. Son, *Journal of High Energy Physics* **2016**, 10.1007/jhep01(2016)021 (2016).
- [69] C. F. Hirjibehedin, I. Dujovne, A. Pinczuk, B. S. Dennis, L. N. Pfeiffer, and K. W. West, *Phys. Rev. Lett.* **95**, 066803 (2005).
- [70] X. Shen, C. Wang, X. Hu, R. Guo, H. Yao, C. Wang, W. Duan, and Y. Xu, *arXiv e-prints*, arXiv:2412.01211 (2024), arXiv:2412.01211 [cond-mat.str-el].

**SUPPLEMENTAL MATERIAL FOR
SPECTRA OF MAGNETO-ROTON AND CHIRAL GRAVITON MODES OF FRACTIONAL CHERN INSULATOR**

In this supplemental material, we provide the details of DMRG and TDVP implementations, more data about the ground state phase diagram of our FCI model, focusing on the FCI-Solid I and Solid I-Solid II transitions, and the spectra of the charge neutral modes and single-particle mode along different paths other than those shown in the main text.

Section I: DMRG and TDVP implementation details

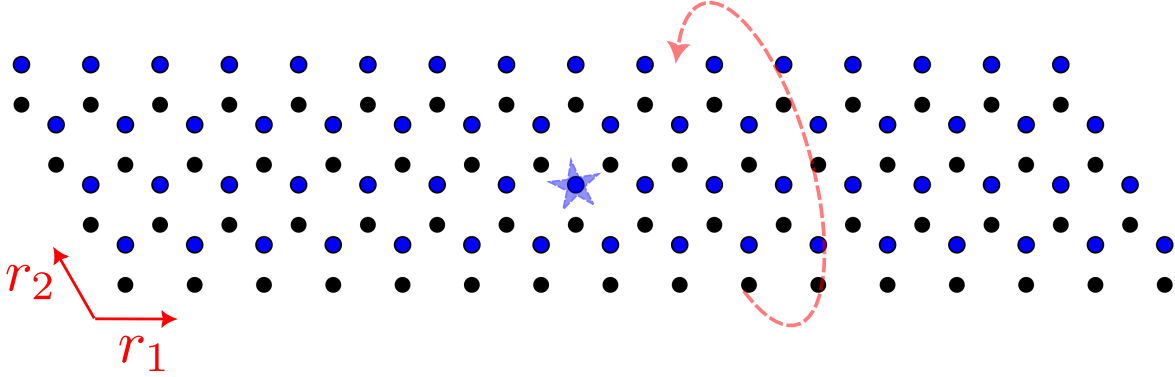


Figure S1. Configuration of 4×16 cylinder with periodic boundary condition along the \mathbf{r}_2 direction. The start is the location of \mathbf{r}_0^A .

In this section, we describe the configuration of the finite honeycomb lattice under investigation and the details of DMRG and TDVP simulations.

Fig. S1 displays the $N_1 \times N_2 \times 2 = 16 \times 4 \times 2$ cylinders that our calculation mainly based on. The black and blue dots label the A and B sub-lattices, respectively. We impose periodic boundary condition along \mathbf{r}_2 direction and open boundary condition along \mathbf{r}_1 direction. The blue star labels the position of \mathbf{r}_0^A where we act an excitation (e.g. n_0^A) on ground state and time evolve the wave function. We use the same \mathbf{r}_0^A for the calculation of $S^A(\mathbf{k}, \omega)$, $G^A(\mathbf{k}, \omega)$ and $g^\pm(\mathbf{k}, \omega)$.

Charge $U(1)$ symmetry is implemented in both DMRG and TDVP calculation based on the TensorKit package [?]. We keep the bond dimension up to $m = 2700$ states in the DMRG simulation to ensure the maximum truncation error below 10^{-5} . In TDVP simulation, we keep up to $m = 250$ states ensuring maximum truncation error below 6×10^{-4} , and time evolve wavefunction $N_t = 2000$ steps with $\Delta t = 0.05$, resulting energy resolution $\Delta\omega = \frac{1}{N_t \Delta t} = 0.01$ upto $\max(\omega) = \frac{1}{\Delta t} = 20$, we set $\hbar = 1$ in time evolution.

We discuss in detail the convergence of DMRG and TDVP simulation with bond dimension in the following section.

Section II: Convergence of DMRG simulation and TDVP numerical stabilization

In this section we show the convergence of the entanglement entropy S_E of the ground state in the FCI, Solid I and Solid II phases.

As shown in Fig. S2 (a), the S_E of the ground state wave function in the FCI phase saturates to constant value along the \mathbf{r}_1 direction as the bond dimension D increases, which is consistent with the fact that the topological ordered state is gapped in the bulk. Fig. S2 (b) and (c) show the S_E in the Solid I and Solid II phases, the oscillations we observed, resemble the charge order inside the CDW phases.

Since our TDVP simulation focuses on the FCI ground state with relatively small bond dimension. We also examine the overlap of the ground state wave function achieved by DMRG at different bond dimensions, the overlap of the ground state wave function is remarkably accurate even in small bond dimension with value $\langle \psi_{D=200} | \psi_{D=1200} \rangle \approx 99.9\%$, which indicates that the MPS in small bond dimension already encodes the majority information of the FCI ground state and greatly facilitate our TDVP simulation.

Next, we show the convergence of the TDVP calculation with respect to the bond dimension and length of cylinder. As well as the fixing scheme we adopt to ensure the stability of the TDVP simulation.

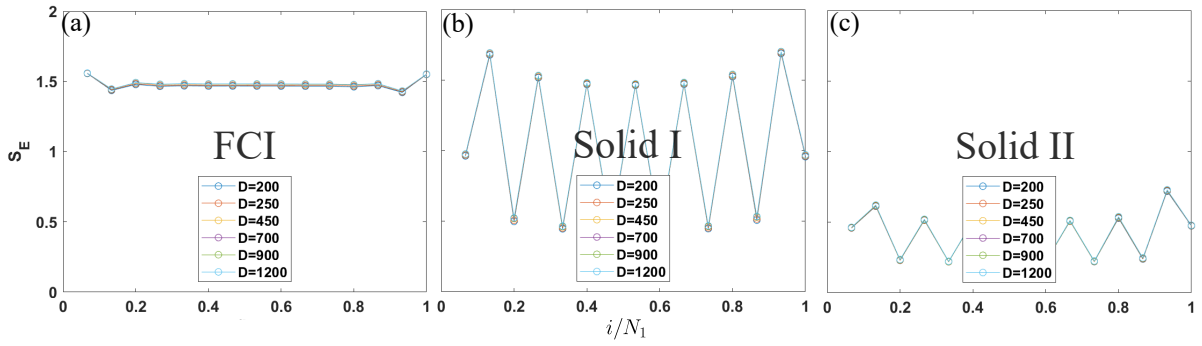


Figure S2. Entanglement entropy of FCI (a) with $V = 1$, Solid I (b) with $V = 3.6$ and Solid II (c) with $V = 4.6$ phases. Here, i measures the distance of the unit cell from the edge of the cylinder along \mathbf{r}_1 direction.

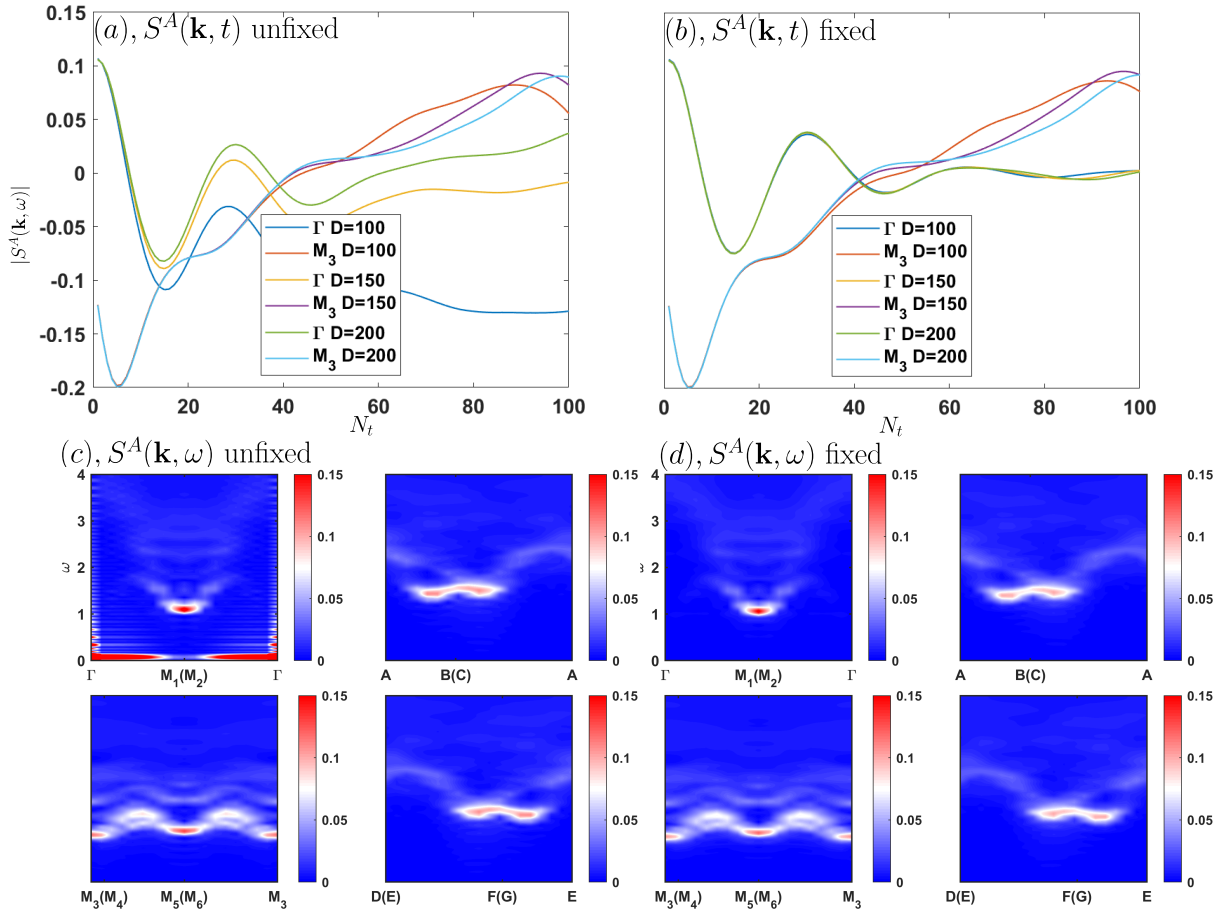


Figure S3. (a), (b) are the time-dependent dynamic density structure factor with a global factor unfixed or fixed, respectively. (c) and (d) represent the respective spectra of (a) and (b). The calculation is done at $V_1 = 4, V_2 = 1$ and the momentum labeling is illustrated in Fig. 1 (d) of the main text.

Bond dimension.— In Fig. S3 (a) and (b), we show the convergence of the dynamic density structure factor with respect to the bond dimension. While in Fig. S3 (a), the $S^A(\mathbf{k} = M_3, t)$ gradually exhibits converged behavior as the bond dimension increases. The $S^A(\mathbf{k} = \Gamma, t)$ behaves differently upon varying bond dimension. Moreover, in Fig. S3 (c), $S^A(\mathbf{k} = \Gamma, \omega = 0)$ present a sharp static peak which is unphysical, since the neutral mode at Γ point represents a global shift of charge density which is contradictory to the conservation of charge. Therefore, in the calculation of $S^A(\mathbf{k}, \omega)$ and $g^\pm(\mathbf{k}, \omega)$, we rescale the canonical center of the matrix product states (MPS) after every TDVP sweep to ensure the amplitude of the wavefunction is

conserved,

$$\langle \psi_0 | \psi(t) \rangle = e^{-iE_0 t} \langle \psi_0 | f(\hat{n}_{\{i\}}) | \psi_0 \rangle \quad (\text{S1})$$

where $|\psi_0\rangle$ is the ground state, $|\psi(t)\rangle$ is the time evolved state which initially is $f(\hat{n}_{\{i\}})|\psi_0\rangle$ at time t , E_0 is the ground state energy, $f(\hat{n}_{\{i\}})$ represent any combination of neutral excitation operator. The right hand side of the equation can be determined before the TDVP simulation, then be used to assist the stability of TDVP. We note that such fixed scheme not only fix the norm of the wave function but also the global phase, which is crucial for the determination of the energy gap.

The spectrum of the fixed and unfixed dynamic density structure factor are shown in Fig. S3 (c) and (d), respectively. The unphysical static peak at Γ point is removed in the fixed scheme while the other gapped mode remains its' shape and position unchanged. This could also be seen from the comparison of $S^A(\mathbf{k} = \mathbf{M}_3, t)$ between Fig. S3 (a) and (b), where they almost have the same manner as time evolves. The first roton gap Δ_{n_1} that is invisible due to the sharp weight of static peak in Fig. S3 (c) can be clearly seen in the fixed scheme Fig. S3 (d). For the calculation of $G^A(\mathbf{k}, \omega)$, we fix the norm of the wave function in the same way.

Length of cylinder.— We also increase the length (N_1) of the cylinder to ensure the convergence of the roton gaps Δ_{n_1} and Δ_{n_2} . As shown in Fig. S4, the roton gaps Δ_{n_1} and Δ_{n_2} are robust as the cylinder length increases, which is consistent with the fact that the roton mode is a bulk excitation in the FCI phase, and exclude the possibility of finite size and boundary effects in our calculation.

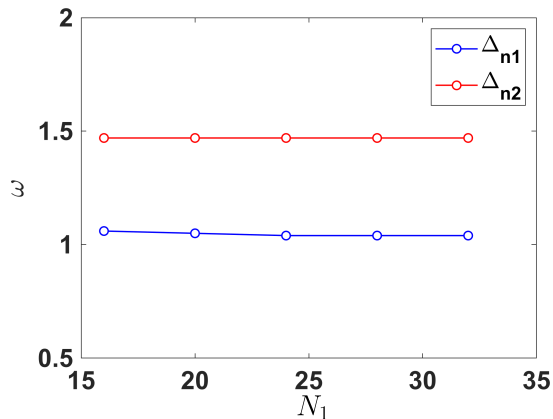


Figure S4. $V_1 = 4, V_2 = 1, D = 200$, as the cylinder length increase. Δ_{n_1} and Δ_{n_2} are robust as the cylinder length increases.

Section IV: FCI-Solid I and Solid I-Solid II transitions

In this section, we determine the phase boundary between FCI, Solid I and Solid II based on DMRG calculation. Fig. S5 (a) and (b) are the static charge order and density structure factor measured at \mathbf{M}_1 point. In FCI-Solid I phase transition, the roton mode at \mathbf{M}_1 goes soft near phase boundary and gives rise to the charge order at \mathbf{M}_1 in Solid I phase, as observed from the formation of charge order (Fig. S5 (a)) and the associated peak of density structure factor (Fig. S5 (b)).

Similar feature of roton-driven phase transition is observed in Solid I-Solid II phase transition, as shown in Fig. S5 (c) and (d). The roton mode at $\mathbf{b}_1/4 + \mathbf{b}_2/2$ goes soft near phase boundary and give rise to the charge order at the same momentum in Solid II phase.

Thus we conclude that the transition points of FCI-Solid I and Solid I-Solid II phase transition are around $V_2 = 3.1$ and $V_2 = 4$ along the fixed $V_1 = 4$ path, respectively.

Section V: Spectra along different paths in BZ

In this section we show the spectra of the single-particle excitation $G^A(\mathbf{k}, \omega)$ along 4 different paths in the BZ in Fig. 1 (d) of the main text.

The single particle spectrum $G^A(\mathbf{k}, \omega)$ along the 4 paths are shown in Fig. S6. The spectrum weights mainly concentrate at the minimal charge gap near Γ point. We note that in our honeycomb lattice model, the band gap of the tight-binding Hamiltonian

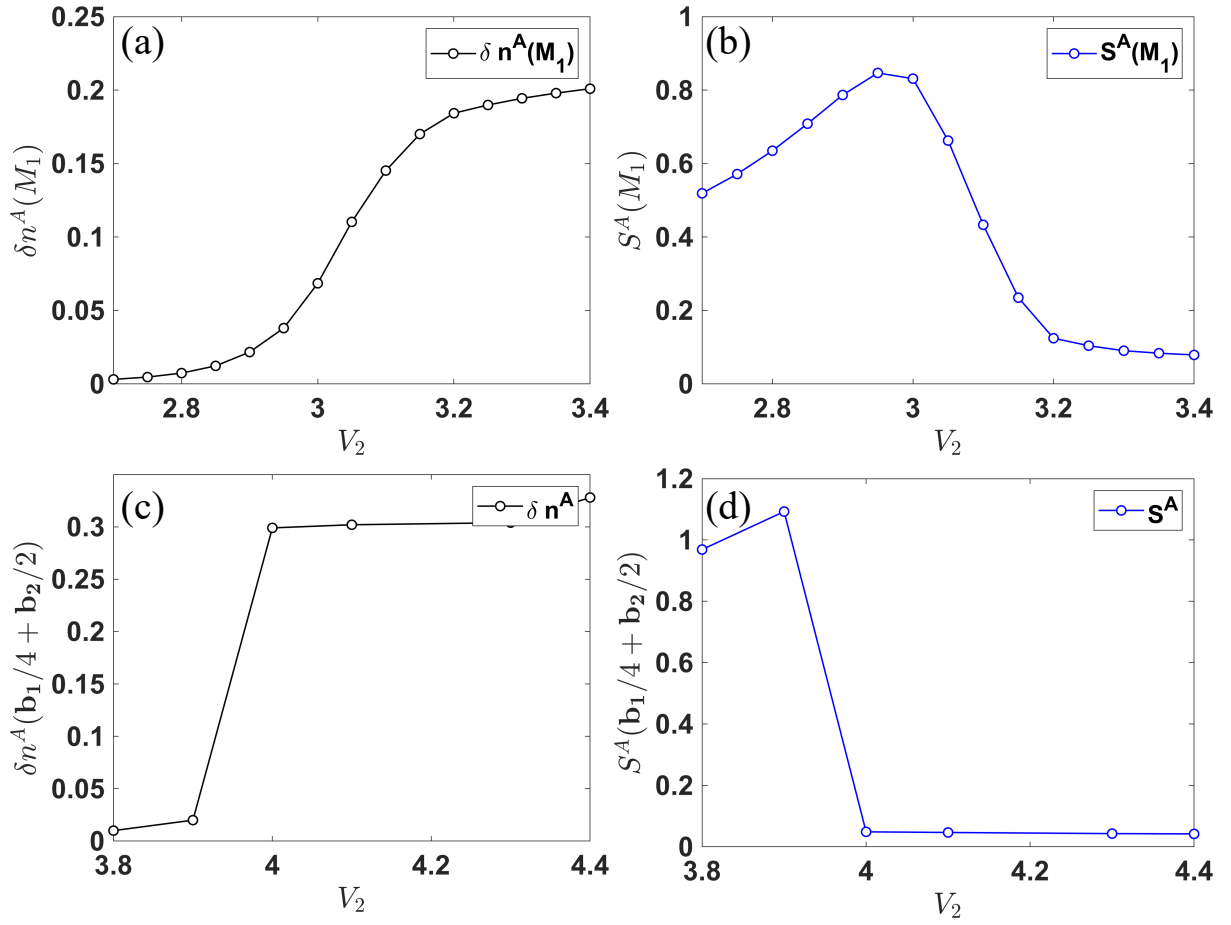


Figure S5. FCI-Solid I transition with charge order $\delta n^A(M_1)$ (a) and static density structure factor $S^A(M_1)$ (b). (c) and (d) are the $\delta n^A(M_1)$ and $S^A(k)$ measured at $b_1/4 + b_2/2$.

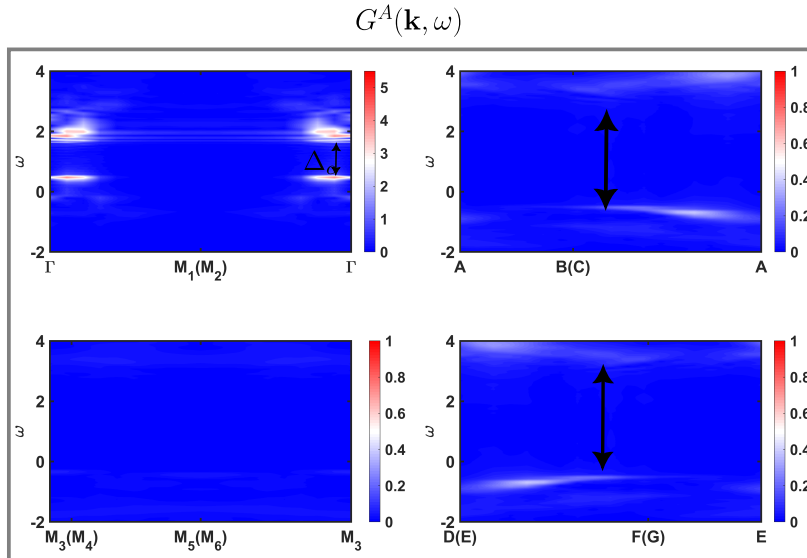


Figure S6. Single-particle spectrum inside the FCI phase ($V_1 = 4, V_2 = 1$) plotted along the 4 paths. The spectrum weight mainly concentrate at the minimal charge gap near Γ point. The charge gap minimum at different paths is labeled with black arrows.

is around 2.5 which is larger than the roton gaps Δ_{n_1} and Δ_{n_2} , while the charge gap is comparative to the band gap as shown in

Fig. S6.

Section VI: Evolution of roton gaps inside FCI phase

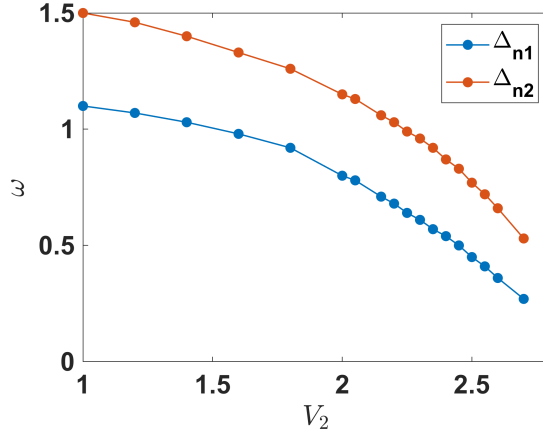


Figure S7. Evolution of the roton gaps in FCI phase. Δ_{n_1} and Δ_{n_2} represent the first and second roton gaps respectively. Their energies become lower while approaching the FCI-Solid I phase boundary.

In this section, we trace the evolution of the roton gaps Δ_{n_1} and Δ_{n_2} as the system approaches the phase boundary. As shown in Fig. S9, the roton gaps Δ_{n_1} and Δ_{n_2} gradually decrease as the system approaches the phase boundary, which is consistent with the fact that the roton mode go soft near the phase boundary and give rise to the charge order in the CDW phase. Δ_{n_2} always remain larger than Δ_{n_1} and as discussed in the main text, it will trigger the transition from Solid I to Solid II after the condensation of Δ_{n_1} .

Section VII: Charge gap identification

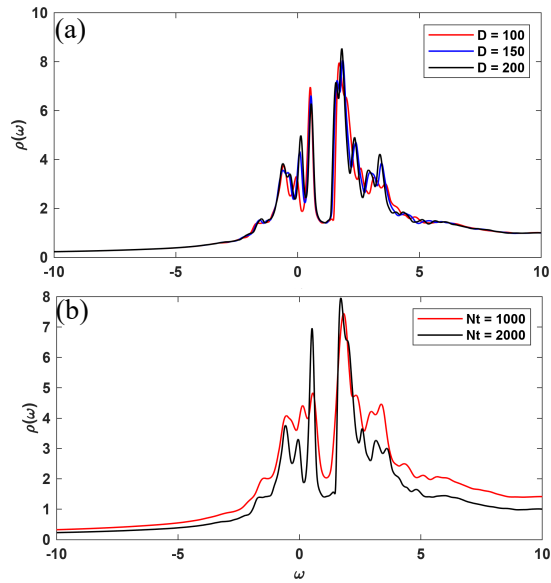


Figure S8. Comparison of the density of states with different MPS bond dimensions(a), and the time evolution length (b). The weights inside the charge gap decreases as the evolution time length increases.

In the main text, we show the single-particle spectrum and the density of states. While there are finite weight inside the charge

gap we identified, we show in this section that such finite weight is attributed to the finite time evolution length of TDVP. As shown in Fig. S8(a), The distribution of energy levels stays stable as the MPS bond dimension increases, while the weight of the charge gap is reduced as the time evolution length increases, as shown in Fig. S8(b). This indicates that the finite weight inside the charge gap is due to the finite time evolution length of TDVP.

Section VIII: Benchmark with exact diagonalization(ED)

To verify the accuracy of the TDVP calculation method, we use the ED Lanczos method to compute the local density of states within a $4 \times 4 \times 2$ cylindrical geometry for comparative analysis. The dynamic Green's function in this context can be represented by a continued fraction expansion within the tridiagonal basis of the Hamiltonian, employing the Lanczos iterative technique. This approach allows for a straightforward calculation of real-frequency correlation functions. During our calculations, we set the Lorentz broadening factor to $\eta = 0.05t_1$. We Fourier transform the real-frequency correlation function to obtain the retard Greens function $G_{ii}(t) = \langle b_i^\dagger(t)b_i \rangle + \langle b_i b_i^\dagger(t) \rangle$ where i site locates at A sublattice of $(m = 2, n = 2)$ th unitcell.

Our findings demonstrate that the results derived from the TDVP method are quantitatively consistent with those obtained using the ED method.

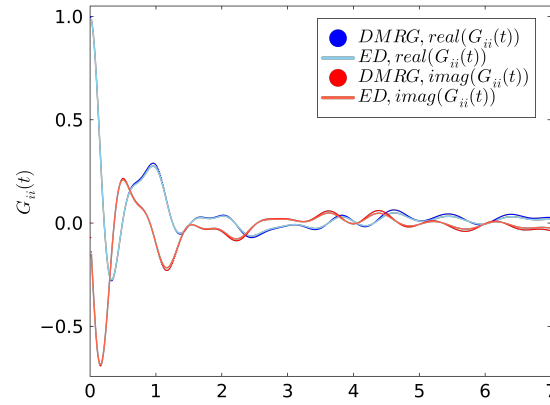


Figure S9. Time evolution of the real space correlation function $G_{ii}(t)$ for a $4 \times 4 \times 2$ cylindrical geometry. The results obtained using the TDVP method are consistent with those derived from the ED method.